



## Development and application of a multi-scale modelling framework for urban high-resolution NO<sub>2</sub> pollution mapping

Zhaofeng Lv<sup>\*</sup>, Zhenyu Luo<sup>\*</sup>, Fanyuan Deng, Xiaotong Wang, Junchao Zhao, Lucheng Xu, Tingkun He, Huan Liu<sup>\*</sup>, Kebin He

5 State Key Joint Laboratory of ESPC, School of Environment, Tsinghua University, Beijing 100084, China

<sup>\*</sup>Z. Lv. and Z. Luo. contributed equally to this work.

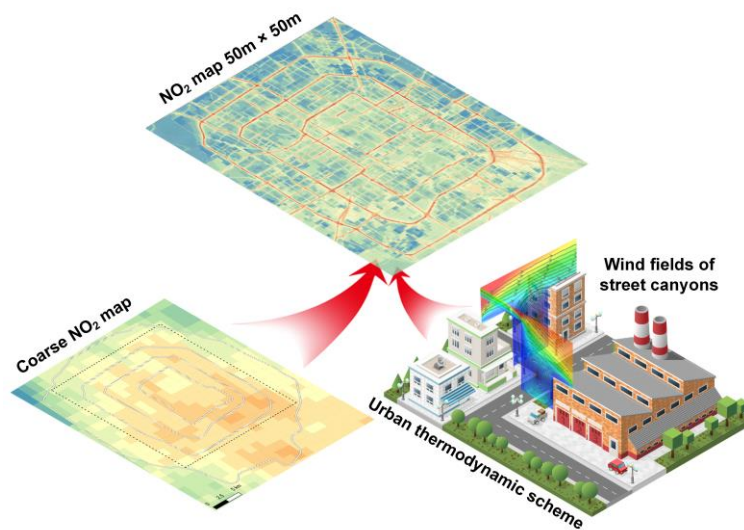
Corresponding Author:

\*Phone and fax: 86-10-62771679; e-mail: [liu\\_env@tsinghua.edu.cn](mailto:liu_env@tsinghua.edu.cn).

10 **Abstract.** Vehicle emissions have become a major source of air pollution in urban areas, especially for near-road environments, where the pollution characteristics are difficult to be captured by a single-scale air quality model due to the complex composition of the underlying surface. Here we developed a hybrid model CMAQ-  
15 RLINE\_URBAN to quantitatively analyse the effects of vehicle emissions on urban roadside NO<sub>2</sub> concentrations at a high spatial resolution of 50 m × 50 m. To estimate the influence of various street canyons on the dispersion  
of air pollutants, a Machine Learning-based Street Canyon Flow (MLSCF) scheme was constructed based on  
Computational Fluid Dynamic and ensemble learning methods. The results indicated that compared with the  
CMAQ model, the hybrid model improved the underestimation of NO<sub>2</sub> concentration at near-road sites with MB  
changing from -10 µg/m<sup>3</sup> to 6.3 µg/m<sup>3</sup>. The MLSCF scheme obviously increased concentrations at upwind  
20 receptors within deep street canyons due to changes in the wind environment caused by the vortex. In summer, the  
relative contribution of vehicles to NO<sub>2</sub> concentrations in Beijing urban areas was 39% on average, similar to results  
from CMAQ-ISAM model, but increased significantly with the decreased distance to the road centerline, especially  
reaching 75% on urban freeways.



## Graphical abstract.





## 1 Introduction

The accelerated urbanization leads to severe air pollution in China. As one of the indicators of air pollution, nitrogen dioxide (NO<sub>2</sub>) causes an adverse impact on human health and promotes the generation of ozone and particulate matter (Pandey et al., 2005; Khaniabadi et al., 2017). During the last decade, benefiting from the implementations  
30 of several air pollution control strategies by the Chinese government, the air quality has improved (Jin et al., 2016; Zheng et al., 2018), and the vertical column densities of NO<sub>2</sub> displayed a decreasing trend after 2013 (Cui et al., 2021) (Shah et al., 2020). However, the economic development and nitrogen oxides (NO<sub>x</sub>) emissions are not decoupled in China (Luo et al., 2022a), and the NO<sub>2</sub> pollution is still much more severe than that in developed  
35 countries. In some megacities of China, such as Chengdu, the daily averaged NO<sub>2</sub> concentration could reach 200 µg/m<sup>3</sup> (Zhu et al., 2019), far exceeding the 24-h average air quality guideline of 80 µg/m<sup>3</sup> suggested by the Ministry of Environmental Protection of China (Mepc, 2012).

The improvement of air quality in China was mainly due to the emission reduction and control measures of industrial and domestic sources (Zhang et al., 2019b), of which the reduction potential has been gradually declining.  
40 Meanwhile, as the population of vehicles is growing rapidly, vehicle emissions have become a major source of NO<sub>2</sub> pollution, especially in urban areas (Luo et al., 2022b), accounting for more than 30% in Lyon (Nguyen et al., 2018). Due to the low release height of vehicle emissions, it is difficult for pollutants to diffuse near the street, and there will be significant accumulation around the source. According to roadside observations, within the distance of about 100-200 m near roads, the concentrations of CO, NO<sub>2</sub>, ultrafine particulate matter (UFP), PM<sub>2.5</sub>, PM<sub>10</sub>,  
45 and other pollutants will increase with the decreased distance to the road centerline, especially for the pollution levels of NO<sub>2</sub> and UFP increasing exponentially. Therefore, the gradient of concentration around the road changes dramatically (Nayeb Yazdi et al., 2015; Hagler et al., 2012). Moreover, the dispersion of air pollutants in the near-road environment is significantly affected by geometric characteristics of the street canyon. For example, in a  
50 standard street canyon, when the external wind direction at the roof level is perpendicular to the street axis, a clockwise vortex will be generated inside, resulting in the accumulation of pollutant concentrations at the upwind receptors in the street canyon (Oke, 1988; Manning et al., 2000). Consequently, how to quantitatively identify urban vehicle-induced air pollution around roads affected by complex underlying surface conditions has become an urgent scientific issue.

55 Regional-scaled air quality models, represented by Chemical Transport Models (CTMs) including Community Multi-scale Air Quality (CMAQ) model (Byun and Schere, 2006), Comprehensive air quality model with



60 extensions (CAMx), and Weather Research and Forecasting/Chemistry model (WRF-Chem) (Grell et al., 2005), has been used extensively in assessment on the impacts of vehicle emissions on the regional atmospheric environment, focusing on the source apportionment (Luo et al., 2022b; Vara-Vela et al., 2016; Kheirbek et al., 2016; He et al., 2016) and evaluation of control measures (Zhang et al., 2020; Yu et al., 2019; Cheng et al., 2019; Ke et al., 2017). However, the spatial resolution of CTMs is generally larger than 1 km×1 km, thus the significant impacts of vehicle emissions on near-source air quality cannot be predicted by CTMs due to the grid homogenization on vehicle emissions.

65 To avoid the aforementioned disadvantages, the local-scaled numerical models based on Gaussian diffusion theory or computational fluid dynamic (CFD) are adopted by numerous researches to study at a finer spatial resolution (Zhang et al., 2021; Patterson and Harley, 2019; Soulhac et al., 2012), using Research LINE-source Dispersion Model (RLINE) (Snyder et al., 2013), Operational Street Pollution Model (OSPM), AERMOD (Cimorelli et al., 2005), and RapidAir® (Masey et al., 2018), etc. However, the large uncertainties in predictions from Gaussian  
70 dispersion models come from the provided meteorological conditions and background concentrations. The natural logarithm function is usually used to characterize the vertical profile of wind speed in both the inertial and rough sublayers, neglecting the influence of urban complex underlying surface compositions on the wind field (Cimorelli et al., 2005; Masey et al., 2018; Snyder et al., 2013). Nevertheless, in standard and deep street canyons, the changes of vertical wind profile cannot be described by the logarithmic form, otherwise the actual wind speed will be greatly  
75 overestimated (Soulhac et al., 2008). Although the OSPM has performed a large number of comparisons with field observations in shallow or standard street canyons, the validation of model performance in deep street canyons with a large aspect ratio was still absent (Kakosimos et al., 2010). Moreover, Murena et al. pointed out that OSPM overestimated the bottom wind speed in a deep street canyon by about 10 times compared with the predictions from CFD, thus greatly underestimating pollutant concentrations (Murena et al., 2009). Comparatively speaking, CFD  
80 models can accurately simulate the flow field and pollutant concentration in complex street canyons, but the simulation domain of CFD models is much smaller than the urban scale, and the influence of the long-term meteorological boundary conditions cannot be considered. Therefore, it is essential to build a model to predict long-term near-road air pollution suitable for the urban complex underlying surface environment.

85 In this paper, we developed a hybrid model CMAQ-RLINE\_URBAN by offline coupling the local RLINE model with the regional CMAQ model and some localized urban thermodynamic parameter schemes, to simulate the near-road NO<sub>2</sub> pollution and quantify the impacts of vehicle emissions at a high spatial resolution. Specifically, in order



to predict the effects of urban street canyons on the diffusion of pollutants, we developed a Machine Learning-based Street Canyon Flow (MLSCF) parameterization scheme, which was based on an ensemble learning method using wind data from 1,600 CFD simulations. To evaluate the performance of CMAQ-RLINE\_URBAN, simulations under several scenarios were conducted in Beijing urban areas from August 1st to 31th of 2019, and validated through comparison with observations from monitoring sites. Furthermore, spatial distribution characteristics of NO<sub>2</sub> concentrations in the near-road environment were also analysed in this study.

## 2 Materials and Methods

### 95 2.1 Hybrid model framework

Based on FORTRAN and R languages, we developed a multiscale air quality hybrid model on the Linux platform, to achieve a high-resolution NO<sub>2</sub> pollution mapping in urban areas. The framework of CMAQ-RLINE\_URBAN was shown in Figure 1. The hybrid model was constructed based on RLINE model, offline coupling with the gridded meteorological field provided by WRF model and the pollutant background concentrations from non-vehicle sources provided by CMAQ model with the Integrated Source Apportionment Method (ISAM), considering the thermodynamic effects caused by the complex underlying surface compositions of the city. In our model, a NO<sub>2</sub> pollution map with a high temporal (1 h) and spatial resolution (<100 m×100 m) can finally be obtained.

The simulation for local meteorological conditions in CMAQ-RLINE\_URBAN included three steps: Estimation for areas above the top of Urban Canopy Layer (UCL), inside of UCL, and inside of the street canyon. (1) In this study, the configuration of WRF model referred to Lv et al. (2020), and the height of midpoint in the bottom layer to the ground was about 22.5 m, which was close to the average height of buildings on both sides of street canyons in urban areas of Beijing. Therefore, the meteorological field simulated by the WRF model was used as the wind field and atmospheric stability at the top of UCL. During the hybrid model running, the meteorological conditions over buildings near each road were obtained separately from the WRF model according to the road location. (2) Then, the surface roughness length ( $z_0$ ) of each road was estimated based on the surrounding building data and used to recalculate the localized meteorological parameters (e.g. Monin-Obukhov length) within UCL according to the algorithm proposed by Benavides et al. ( $z_0$  scheme) (2019). The atmospheric turbulence intensity in urban areas around sunset in the afternoon was enhanced considering the influence of the urban heat island (Kheirbek et al.) (Kheirbek et al.) effect based on the method in Air Quality Dispersion Modeling (UHI scheme)(Cimorelli et al., 2005). (3) Finally, the wind field within UCL was calculated according to different types of road environments: open terrain and street canyon. The logarithmic wind profile based on Monin-Obukhov Similarity Theory (MOST) (Foken, 2006) in the original RLINE model was still used when the receptor was located in the open terrain (MOST



scheme), while the MLSCF parameterization scheme was used for receptors in the street canyon to quantitatively  
120 characterize the influence of the street canyon geometry and the external wind environment at the top of the roof.  
The detailed introduction for street canyon geometry and the MLSCF scheme was described in the following  
section.

The real-time vehicle emission inventory based on Street-Level On-road Vehicle Emission (SLOVE) Model  
125 developed in our previous study (Lv et al., 2020), which was based on the real-time traffic condition data from  
AMap ([www.amap.com](http://www.amap.com)), was used in both regional and local air quality models. In our simulation, the  
concentrations of NO, NO<sub>2</sub>, and O<sub>3</sub> excluding contributions from vehicle emissions were used as background  
concentrations at the roof level, avoiding the double counting in the coupling process. These background  
concentrations were simulated by CMAQ-ISAM model, in which the emissions were divided into mobile and other  
130 four emission groups to trace their contributions separately, and details were presented in our previous study (Lv  
et al., 2020). In addition, the influence of atmospheric turbulence and building geometry on the vertical mixing of  
background concentration was considered (vertical mixing scheme). The ratios of wind speed at surface and roof  
levels were used as a proxy to calculate the contribution of background concentration over street canyons to the  
near-ground receptors (Benavides et al., 2019). Finally, combined with the vehicle-induced primary NO<sub>x</sub>  
135 concentration calculated by the RLINE kernel, the high spatial resolution NO<sub>2</sub> map could be simulated considering  
the photochemical process of NO<sub>x</sub>. In this study, a simplified two-reaction scheme was incorporated into the RLINE  
model to characterize the photochemical process of NO<sub>x</sub>, which has been successfully applied to the SIRANE  
dispersion model (Soulhac et al., 2017).

## 140 2.2 Development for MLSCF scheme

### 2.2.1 The database of street canyon geometry

We first established a database of street canyon geometry for 15,398 roads in urban areas of Beijing based on the  
three-dimensional building data obtained from our previous study (Lv et al., 2020) using Geographic Information  
System (GIS). Three typical parameters to represent street canyon geometry were investigated, including height  
145 ratio ( $H_l/H_r$ ) ( $H_l$  is the building height on the left side, while  $H_r$  is the building height on the right side), aspect  
ratio ( $H/W$ ) ( $H$  is set to be the average height, and  $W$  is the width of the street canyon), the canyon length to height  
ratio ( $L/H$ ) ( $L$  is set to be the length of the street canyon). In this study, the extreme canyon geometry was not  
considered, and the typical street canyons were selected as the following conditions: (1) The proportion of actual  
street canyon length (the length of road where the buildings nearby) was greater than 0.5; (2)  $H/W$  was greater



150 than 0.2; (3)  $H_l/H_r$  was between 0.3 and 3.3. Finally, the total number of the typical street canyon was 1,889, with  
a total length of 787 km. The spatial distributions of canyon geometry were shown in Figure S1. In urban areas of  
Beijing, street canyon width was generally wide with a mean of 50.3 m, and buildings on both sides were relatively  
low with a mean of 23.6 m. Most street canyons were obviously located in areas within the fourth ring road. The  
shallow ( $H/W \leq 0.5$ ) canyons and long canyons ( $L/H > 7$ ) were dominated, accounting for 54% and 84% of the total  
155 number of street canyons.

### 2.2.2 Description of CFD cases

To predict air flow in street canyons comprehensively, CFD simulations were conducted under combinations of  
different values of controlling factors based on ANSYS FLUENT (v19.2). The controlling factors included the  
160 aforementioned three typical parameters to represent canyon geometry and the background wind speed at the height  
of  $H$  ( $V(H)$ ) as well as its direction ( $\alpha$ ) to describe the external wind environment. The selected values of each  
factor were listed in Table 1, and total 1600 (i.e.,  $5 \times 4 \times 4 \times 5 \times 4$ ) simulations were implemented.

In this study, the computational domain of three-dimensional (3D) full-scale CFD simulations was shown in Figure  
165 2. The average building height  $H$  of the street canyon was always set to 21 m in different simulations, which was  
similar to the mean street canyon height in Beijing. Other actual size of street canyons (e.g. street canyon width  $W$ )  
was calculated according to the ratio of each specific scenario. Distances between urban canopy layers (UCL)  
boundaries and the domain top, domain inlet and domain outlet were set as  $5H$ ,  $6H$ , and  $20H$ , respectively.  
Following the CFD guideline (Tominaga et al., 2008; Franke et al., 2011), zero normal gradient conditions or  
170 pressure outlet conditions were applied at the domain outlet, and symmetry boundary conditions were adopted at  
the domain top and two lateral domain boundaries. For near-wall treatment, no-slip wall boundary conditions with  
standard wall functions were used (Fluent, 2006). All governing equations for the flow and turbulent quantities  
were discretized by the finite volume method with the second-order upwind scheme. The SIMPLE scheme was  
used for the pressure and velocity coupling. The residual for continuity equation, velocity components, turbulent  
175 kinetic energy, and its dissipation rate were all below  $10^{-5}$ . Meanwhile, the CFD simulation would also stop when  
the iteration steps exceeded 10,000, due to the large computing cost of so many simulations. The selected turbulence  
model and grid arrangement were discussed in the following section.



At the domain inlet, the power-law velocity profile (Brown et al., 2001), vertical profiles of turbulent kinetic energy  
180  $k_{in}$  and its dissipation rate  $\varepsilon_{in}$  at the domain inlet (Lien and Yee, 2004; Zhang et al., 2019a), were described below:

$$U_0(z) = U_{ref} \left( \frac{z}{H_{ref}} \right)^\alpha$$

$$k_{in}(z) = (I_{in} \times U_0(z))^2$$

$$\varepsilon_{in}(z) = \frac{C_\mu^{3/4} k_{in}^{3/2}}{\kappa z}$$

Here,  $U_0(z)$  stood for the stream-wise velocity at the height  $z$ .  $U_{ref}$  represented the reference speed. The reference  
185 height  $H_{ref}$  was 21m. The power-law exponent of  $\alpha=0.22$  denoted underlying surface roughness above medium-  
dense urban area (Kikumoto et al., 2017). Turbulence intensity  $I_{in}$  was 0.1, Von Karman constant  $\kappa$  was 0.41 and  
 $C_\mu$  was 0.09.

### 2.2.3 The CFD validation

190 In this study, the stream-wise and vertical velocity predicted by CFD within street canyons was compared with  
wind tunnel data in previous researches. For buildings of the cube arrays model, wind tunnel data from Brown et  
al. (2001) was used to evaluate the reliability of CFD results by measuring vertical profiles of velocity. For long-  
street models, we predicted horizontal profiles of velocity along the street centerline at the height of  $z=0.11H$  or  
vertical profiles at some points and then validated CFD simulations using wind tunnel data from Hang et al. (2010).  
195 The description and validation results were shown in Figure S2-S3, and Table S1, respectively.

We identified the influence of different minimum sizes of hexahedral cells near wall surfaces (fine: 0.1m, medium:  
0.2m, and coarse: 0.5m) and turbulence models (standard k- $\varepsilon$  model and RNG k- $\varepsilon$  model) on the predicted velocity,  
to evaluate the grid independence and turbulence model accuracy (Figure S3). The results indicated that the  
200 predictions from the standard k- $\varepsilon$  model could well match the variations of observed velocity within the street  
canyon, of which performances were much better than that of the RNG model. In addition, different grid resolutions  
used in simulations would not significantly affect the predicted results. We finally adopted the standard k- $\varepsilon$  model  
to characterize turbulence, and the grid with an expansion ratio of 1.1 was applied in which the minimum size of  
hexahedral cells near wall surfaces was 0.5 m to save the computing cost.

205

Moreover, the averaged wind speed from CFD in street canyons with different aspect ratios and external wind





direction was compared with predictions from other empirical methods used in SIRANE model (Soulhac et al., 2012) and MUNICH model (Kim et al., 2018). Similar predictions using different methods also proved the reliability of CFD simulation in this study (Figure S4).

210

#### 2.2.4 Machine learning

Finally, based on the database including 42,880 samples obtained from 1600 CFD simulations, the Random Forest (RF) and Multivariate Adaptive Regression Splines (MARS) were both used to simulate the wind vector along X-axis ( $V_x$ ) and Y-axis ( $V_y$ ) at different heights within the street canyon respectively. The input predictor variables included  $H/W$ ,  $L/W$ ,  $H_l/H_r$ , the receptor relative height ( $z/H$ ), the background wind vector at the height of H along X-axis ( $Vbg_x = V(H) \times \sin \alpha$ ) and Y-axis ( $Vbg_y = V(H) \times \cos \alpha$ ). RF model algorithm is an ensemble learning method that generates many decision trees and aggregates their results, which has been developed to solve the high variance errors typical of a single decision tree (Breiman, 2001). MARS is a nonparametric and nonlinear regression method, which can be regarded as an extension of the multivariate linear model. An ensemble learning method combined with the advantages of these two machine learning models was used as the MLSCF scheme to predict wind environment in street canyons and incorporated into the hybrid model, which was discussed in the section 3.1.

In RF model, the number of predictors randomly sampled at each split node in the decision tree ( $m_{try}$ ) and the number of trees to grow ( $NumTrees$ ) are two important hyperparameters that determine the performance of the model. Similarly, in MARS model, the two important hyperparameters are the total number of terms ( $nprune$ ) and the maximum number of interactions ( $degree$ ). By comparing the mean squared error (MSE) for testing datasets across models with candidate parameter combinations, we set  $m_{try}$  and  $NumTrees$  as 6 and 200, respectively, and  $nprune$  and  $degree$  as 23 and 3, respectively. Additionally, the 10-fold cross-validation (CV) repeated ten times were considered to evaluate the prediction performance of our models. The total dataset was randomly divided into 10 subsets, where 9 subsets was used to train model and another was applied for validation.

In order to identify the sensitivity and response relationship between prediction variables and results in RF model, we used the MSE for out-of-bag (OOB) to evaluate the relative importance of each feature to  $V_x$  and  $V_y$ , by randomly replacing the value of a single prediction variable one by one (Liaw, 2002). Higher values of increase in MSE indicated that the predictor was more important. In addition, Partial Dependence Plots (PDPs) was applied to

235



establish the response relationship between the change of a single predictive variable and the predicted results, considering the average influence of other variables (Greenwell, 2017).

### 240 2.3 Configuration of CMAQ-RLINE\_URBAN

The simulations for the near-ground NO<sub>2</sub> concentrations were conducted from August 1st to 31th in 2019 when the photochemical reactions were strong. The simulation domain for the hybrid model covered the core urban areas within and surrounding the fifth ring road, shown in Figure 3. The receptors included both grids and observation stations. The grid receptors were set at a spatial resolution of 50 m×50 m, and the height above the ground was 1.5  
245 m, which was equivalent to the height of the human breathing. We used data from 10 observation stations located in the normal urban environment and 5 near-road monitoring sites for validation (Beijing Ecological Environment Monitoring Center, available at <http://zx.bjmemc.com.cn/>) (DSH, NSH, QM, XZM, and YDM) in the simulation domain (Figure 3), which were 10 meters and 3 meters above the ground respectively. The QM and XZM sites were located in shallow street canyons, and details for the morphometric of near-road measurement sites were  
250 shown in Table S2.

In general, compared to the RLINE model, CMAQ-RLINE\_URBAN has the following improvements:

- (a) The gridded meteorological parameters provided by WRF model were used.
- (b) Gridded non-vehicle-related concentrations provided by CMAQ-ISAM model were used as background  
255 concentrations.
- (c) A simple NO<sub>x</sub> photochemical scheme was incorporated to simulate NO<sub>2</sub> concentrations.
- (d) Thermodynamic effects caused by the special underlying surface structures of the city were considered, including UHI effects and the influence of local buildings on turbulence intensity and vertical mixing of background concentrations.
- 260 (e) A newly developed MLSCF scheme was applied to predict wind environment in street canyons.

In our simulation, the model configurations in the base scenario CMAQ-RLINE\_URBAN included all (a)-(e) schemes, and the other two control scenarios were set to investigate the sensitivity of urban schemes on predictions, where all input data was set to be the same. The scenario CMAQ-RLINE only including (a)-(c) schemes was set to  
265 analyze the impacts of urban thermodynamic schemes, and the scenario CMAQ-RLINE\_URBAN\_nc including (a)-(d) schemes was set to identify the impacts of the MLSCF scheme.



### 3 Results and Discussion

#### 3.1 Fitting results of machine learning

270 In this study, the 10-fold cross-validation (CV) repeated ten times were considered to evaluate the prediction performances of RF and MARS models. As shown in Figure 4 and Figure S5, both models performed acceptable robustness in CV, indicating that neither RF nor MARS model overfitted the data. In general, the performances of both models in predicting  $V_y$  was better than that in  $V_x$  of which the absolute value was relatively small, especially for MARS model. Since  $V_x$  was responsible for the formation of the vortex within street canyons and affected by multiple factors, it was more difficult to be simulated. The averages of mean absolute error (MAE), root mean square error (RMSE), relative error (RE), and correlation coefficient (R) in the CV of the RF model for  $V_x$  and  $V_y$  were 0.04 m/s and 0.05 m/s, 0.02 m/s and 0.03 m/s, 43.0% and 42.5%, and 0.99, respectively. Although the average of the RE was a little high, particularly when the wind speed was low, the medians were relatively low with 9.8% and 2.7%, respectively, indicating a great model performance. Compared with the advanced non-linear RF algorithm, the MARS model performed not very well, especially when the absolute value of  $V_x$  was greater than 1 m/s and  $V_y$  was less than 3 m/s. However, when the predicted wind speed by machine learning methods was compared with observations from wind tunnel experiments, we found that the performance of the MARS model was obviously better than that of RF model in one of validation cases (Figure 5). The decision tree model like RF failed to respond to the parts beyond the range of prediction variables ( $V_{bg,y}=17$  m/s  $\gg$  5 m/s), while the more reasonable predictions can be obtained by the MARS model which used piecewise linear function essentially. Therefore, the MLSCF scheme was established based on an ensemble learning method to combine the advantages of each model. The RF model was used when the input value was within the range of predictors shown in Table 1, otherwise the predictions from the MARS model were used.

290 In addition, the importance of each predictor variable in the RF model was investigated to explain their impacts on predictions. As shown in Figure 6, the background wind speeds on x and y axis played vital roles in predictions of  $V_x$  and  $V_y$ , respectively, followed by the relative height ( $z/H$ ). Among the geometric parameters of the street canyon, the impact of  $L/W$  was least. Since  $V_x$  was the main driving force for the formation of vortices in street canyons, it was more affected by the geometry of street canyons especially  $H_l/H_r$ , comparing to  $V_y$ . This feature importance ranking was basically consistent with the conclusion in a previous study (Fu et al., 2017). Figure S6 showed the PDPs of each predictor variable in RF model for  $V_x$  and  $V_y$ . As  $z/H$  grew,  $V_x$  and  $V_y$  showed linear and logarithmic increase patterns, respectively. And the resistant effect of windward buildings on wind speed enhanced



with the increasing of  $H_l/H_r$ , resulting in an significant decrease in  $V_x$  particularly when  $H_l/H_r$  was lower than 1.25. The relationship between predictors and results in the model was consistent with the actual mechanism, indicating our ensemble model could provide an accurate description of the wind field in the street canyon.

### 3.2 Impacts of MLSCF on simulations in street canyon

We compared the differences between monthly mean wind profile in different street canyons including QM (shallow canyon:  $H/W = 0.22$ ), XZM (shallow canyon:  $H/W = 0.35$ ), SZJ (standard canyon:  $H/W = 1$ ) and JTDL (deep canyon:  $H/W = 1.93$ ), calculated by the default logarithmic function based on MOST in the original RLINE model (Foken, 2006), and the MLSCF scheme developed in this study. As shown in Figure 7(a)-(d), the wind profile estimated by MOST showed a logarithmic change at the height above displacement height ( $d_h$ ) with a decrease to 0 at  $d_h$ , and remained constant below  $d_h$ . Compared with the MOST, the simulated wind speeds near the ground and at the top of canyons were generally lower based on the MLSCF scheme in shallow and standard street canyons. In the deep street canyon, the significant reduction in ventilation volume led to the mean wind speed simulated by the MLSCF scheme much lower than that of MOST at all heights. Although the aspect ratios of the street canyon located in QM and XZM were similar, their orientations were quite different, resulting in significant differences under prevailing external winds in different directions. Since the prevailing northerly and southerly wind was observed in Beijing during the study period, the resistance effect of the buildings on both sides of the east-west street canyon located in QM was more obvious.

We also investigated the impacts of the MLSCF on hourly wind direction at the bottom ( $z = 3m$ ) of different street canyons by comparing the roof-level predictions from WRF model (Figure 7(e)-(f)). In the shallow street canyon like QM, the simulated wind direction at the bottom was consistent with the background on the whole, with the R reaching 0.8. When the background wind direction was less than  $180^\circ$ , the averaged wind direction at the bottom simulated by MLSCF was  $91.8^\circ$ , which was basically consistent with the angle between the street and the south direction ( $84.5^\circ$ ). While when the background wind direction was greater than  $180^\circ$ , the average wind direction predicted by MLSCF ( $257.4^\circ$ ) was similar to that in the opposite direction of the street ( $264.5^\circ$ ), which was in line with the theory proposed by Soulhac et al. (2008) that the average wind direction in street canyons was assumed to be consistent with the (opposite) orientation of the street. While in the deep street canyon of SZJ, when the external wind perpendicularly blew to the street, the wind direction at the bottom was completely opposite to that at the top due to the formation of vortex, with the R reaching -0.97. In conclusion, compared with the traditional MOST

method, the newly developed MLSCF scheme could well simulate the influence of the external wind environment and geometry on the wind field inside the street canyon.

330

As shown in Figure 8, the impacts of the MLSCF scheme on simulated NO<sub>2</sub> concentration were identified by the differences between CMAQ-RLINE\_URBAN and CMAQ-RLINE\_URBAN\_nc scenario during a clean day (August 24th). When the atmosphere was stable at night, in street canyons with a large aspect ratio, the wind direction at the bottom changed to the opposite to that at the top, combined with the decreased wind speed affected by the MLSCF scheme, the NO<sub>2</sub> concentrations at upwind receptors increased by up to 80 µg/m<sup>3</sup>. Meanwhile, the changes in wind direction would also decrease the concentrations at downwind receptors by up to 20 µg/m<sup>3</sup>. For example, in the SZJ standard canyon, the background wind direction over the street was 79° (easterly), and the wind direction at the bottom changed to 291° affected by the MLSCF scheme (westerly). Therefore, the NO<sub>2</sub> concentrations at upwind receptors increased, and the location of peak NO<sub>2</sub> concentration shifted to the upwindward. Since the changes in NO<sub>2</sub> concentrations were also influenced by the local on-road emissions, the increase was only up to 2.1 µg/m<sup>3</sup> in SJZ street, where the traffic flow and vehicle emissions were small at night. However, less influence was observed during the day in the convective boundary layer. During this period, although the wind direction at the bottom was not changed obviously due to the parallel background wind in SZJ street, the increased surface wind speed was beneficial for the dispersion, resulting in the decreased concentration in receptors within both sides of the street canyon. In summary, the MLSCF scheme enabled the characterization of the concentration distribution in street canyons.

335  
340  
345

### 3.3 Performance of near-road simulations from different models

The performances in predicting NO<sub>2</sub> concentrations at all monitoring sites from different models were first compared, including CMAQ-RLINE\_URBAN, CMAQ-RLINE and CMAQ model. The mean bias (MB), RMSE, normalized mean bias (NMB), normalized mean gross error (NMGE), the fraction of predictions within a factor of two (FAC2), Index of agreement (IOA), and R between simulations and observations were all selected as statistical indicators for the evaluation. In general, the performance of CMAQ-RLINE\_URBAN was the best at all urban sites (Table 2). Compared to the CMAQ model, the averaged MB and NMB at urban sites in the hybrid model decreased from 8 µg/m<sup>3</sup> to 1.3 µg/m<sup>3</sup> and 27% to 4%, respectively.

350  
355

Diurnal variations of observed and predicted hourly averaged NO<sub>2</sub> concentrations at near-road sites from different models were mainly compared and shown in Figure 9. The comparison of hourly and daily averaged concentrations



was shown in Figure 10. Overall, the CMAQ-RLINE\_URBAN performed best with the smallest deviations. By  
360 comparing the performances of the CMAQ and CMAQ-RLINE scenario, we found the direct coupling between the  
CMAQ and RLINE models could reproduce the high NO<sub>2</sub> concentrations at near-road sites in daytime, and  
significantly improve the underestimation of near-source concentrations due to grid dilution on emissions in  
CMAQ model. The averaged MB and NMB at all sites changed from -10 µg/m<sup>3</sup> to 25.6 µg/m<sup>3</sup>, and from -20% to  
51%, respectively. However, a significant overestimation was found in the CMAQ-RLINE at night (0:00-6:00) and  
365 around sunset in the afternoon (16:00-23:00), of which the peak could exceed the observed concentrations by more  
than 1 times. This overestimation was reduced in the CMAQ-RLINE\_URBAN, where the urban thermodynamic  
schemes were implemented. The averaged MB and NMB decreased to 6.3 µg/m<sup>3</sup> and 12%, respectively, due to the  
following reasons: (1) The increased surface roughness length slightly enhanced local turbulence intensity near  
roads; (2) The UHI scheme enhanced the intensity of atmospheric turbulence in urban areas before and after sunset  
370 in the afternoon; (3) The effect of turbulence intensity on the local vertical mixing of background concentrations  
was considered, significantly reducing the mixing ratio of concentrations over UCL and near the ground at nights  
in the stable boundary layer (Figure S7), which was probably the main driving force of decreased predictions in  
the hybrid model (Benavides et al., 2019). However, the CMAQ-RLINE\_URBAN slightly overestimated the  
nighttime NO<sub>2</sub> concentration of all observation stations except the DSH, which was probably caused by  
375 overestimations of background concentrations from CMAQ-ISAM and vehicle emissions.

The accuracy of model performances at each traffic site showed a little difference affected by the variations in the  
traffic flow and emissions of nearby roads, as well as the geometry of surrounding buildings and street canyons. At  
DSH and NSH sites, which were adjacent to ring roads as the main urban freight corridors with a high traffic flow  
380 including a large proportion of trucks, the high NO<sub>x</sub> emissions led to the highest roadside NO<sub>2</sub> observations among  
all sites. The CMAQ model would significantly underestimate the high NO<sub>2</sub> concentration at sites nearby ring roads,  
with MB and NMB lower than -15 µg/m<sup>3</sup> and -28% (Table S3), respectively, which was improved using CMAQ-  
RLINE\_URBAN. However, the hybrid model performed a minor overestimation at the NSH site, since the monitor  
was actually positioned in the road centerline but assumed to be located downwind in the model, resulting in a  
385 relatively large systematical error (Snyder et al., 2013). In total, CMAQ-RLINE\_URBAN performed best among  
all models, especially improving the estimation of NO<sub>2</sub> concentrations near roads by the original regional model.

Additionally, Figure S8 showed the comparison between simulated and observed roadside hourly and daily  
maximum 8-hour average O<sub>3</sub> concentrations by different models, and their diurnal variations were shown in Figure



390 S9. Generally, the hybrid model significantly improved the overestimation of daytime O<sub>3</sub> concentrations by the CMAQ model when considering the titration effect of high NO concentration near roads on O<sub>3</sub>. In the hybrid model, the peak time was delayed to about 15:00, which was closer to the observation, but still 1-2 hours earlier than the actual time, which may be related to the uncertainty in NO<sub>2</sub> photolysis rate.

### 395 **3.4 Spatial distribution characteristics of simulated concentrations**

We investigated the differences between the spatial distribution of the monthly averaged NO<sub>2</sub> concentration simulated by the CMAQ and CMAQ-RLINE\_URBAN models, as shown in Figure 11. Since the urban thermodynamic schemes were considered in the hybrid model, the overestimation of most urban environmental receptors by CMAQ model was relieved. Within the fourth ring road and its surrounding areas, the mean  
400 concentration of NO<sub>2</sub> from CMAQ-RLINE\_URBAN was 30.1 µg/m<sup>3</sup>, lower than that from the CMAQ model (39.5 µg/m<sup>3</sup>). The overall spatial distribution characteristics of NO<sub>2</sub> predictions from both models showed that the concentrations in south regions were high due to the pollution transport from Hebei province (An et al., 2019). However, near-road hotspots for the NO<sub>2</sub> pollution were identified in the hybrid model where the spatial resolution of results increased to 50 m×50 m. The NO<sub>2</sub> concentrations nearby ring roads with high traffic flow and emissions  
405 were up to 120 µg/m<sup>3</sup>, much higher than the maximum prediction from CMAQ model (52.4 µg/m<sup>3</sup>). In addition, the simulated near-road concentrations from the hybrid model during traffic peak hours (18:00-19:00) were significantly higher than those at noon (12:00-13:00), while there were few changes in results from CMAQ model (Figure S10).

410 The NO<sub>2</sub> concentrations estimated by CMAQ-RLINE\_URBAN at all receptor grids followed a two-mode Gaussian distribution (Figure S11), which was similar to Zhang's results (Zhang et al., 2021). The NO<sub>2</sub> concentrations as a result of vehicle emissions were further calculated by the differences between the total and background concentrations. In general, the vehicle-induced NO<sub>2</sub> concentrations in urban areas was 11.8 µg/m<sup>3</sup>, accounting for 39% of the total concentrations, which was similar to the predicted contribution from the CMAQ-ISAM model  
415 (42.5%).

Figure 12 showed the changes in NO<sub>2</sub> concentrations simulated by the hybrid model with distance from the receptor to its nearest road centerline. The concentrations at receptors within 200 m from road were significantly affected by vehicle emissions. Within 50 m around the road, as the distance from receptors to the road centerline gradually  
420 increased, the NO<sub>2</sub> concentrations decreased exponentially. The total NO<sub>2</sub> concentrations decreased from 53.1



$\mu\text{g}/\text{m}^3$  to  $30 \mu\text{g}/\text{m}^3$ , and the vehicle-induced concentrations also dropped from  $34.7 \mu\text{g}/\text{m}^3$  to  $12.6 \mu\text{g}/\text{m}^3$ . The concentrations near roads with different types were highly dependent on the emission intensity. The  $\text{NO}_2$  concentration was highest in the center of the urban freeway, which was  $76 \mu\text{g}/\text{m}^3$  and about 1.9 times that on local roads. The relative contribution of vehicle emissions to  $\text{NO}_2$  concentration reached up to 75.3% on urban freeways, as well as 71.9% and 65.5% on artery roads and freeways, but only 51.1% on local roads. It was worth noting that although the  $\text{NO}_2$  concentrations at far receptors to the road on highways were slightly higher than those on other road types, but the contribution of vehicle emissions was the least. It was since the  $\text{NO}_x$  emission intensity of freeways was as high as that on artery roads, but the density and height of buildings around freeways were usually low, resulting in a high vertical flux of background concentrations from the top of UCL to the ground. In conclusion, the results from the hybrid model accurately reflected not only the impacts of local on-road emissions, but also the pollution characteristics affected by non-vehicle sources at the regional scale.

#### 4 Conclusions

In this study, we developed a hybrid model CMAQ-RLINE\_URBAN to quantitatively analyse the effects of vehicle emissions on urban roadside  $\text{NO}_2$  concentrations at a high spatial resolution of  $50 \text{ m} \times 50 \text{ m}$ . The main conclusions of this study are as follows:

The developed MLSCF scheme revealed that affected by the geometry of buildings on both sides of the road, the wind filed in the street canyon sometimes was quite different from that in the environmental background. In deep street canyons, the wind speed at the bottom decreased obviously due to the resistant effect of buildings, and the directions of horizontal flow in bottom and top of the canyon were completely opposite due to the formation of vortex. The application of MLSCF scheme in the hybrid model led to increase  $\text{NO}_2$  concentrations at upwind receptors within deep street canyons due to changes in the wind environment.

The comparison between observations and predictions showed that the hybrid model significantly improved the underestimation of near-source concentrations due to grid dilution on emissions in CMAQ model. The implementation of the urban thermodynamic schemes in the hybrid model also relieved the overestimation in night-time  $\text{NO}_2$  concentration from the CMAQ directly coupled with RLINE model. The predictions from CMAQ-RLINE\_URBAN model could accurately reflect not only the impact of road local emissions, but also the pollution characteristics of non-vehicle sources at regional level. It revealed that in summer, the average contribution of vehicle emission to  $\text{NO}_2$  concentration in urban areas of Beijing was  $11.8 \mu\text{g}/\text{m}^3$ , and the relative contribution



accounted for approximately 39%. Moreover, the vehicle-induced NO<sub>2</sub> pollution increased significantly with the decreased distance to the road centerline, especially reaching 76 µg/m<sup>3</sup> (75%) on urban freeways.

455 On the basis of this study, the following perspectives are proposed for future research: (1) The long-term site-  
observation of wind environment and pollutant concentrations in various street canyons were suggested to be  
compared with modelling results, especially in deep street canyons with large aspect ratio. The navigation  
monitoring technology would be applied in the model verification, which can carry out large-scale observation of  
concentration along streets. (2) Here, we considered the dynamic impact of idealized building structure on wind  
460 environment in street canyons. However, there are many other influencing factors, such as building layout and  
arrangement, roof shape, green vegetation, and thermodynamic effect, which are suggested to be considered in  
future studies. (3) In this study, we mainly focused on the NO<sub>2</sub> concentrations. In fact, the concentration of  
particulate matter, especially UFP, will also have an obvious peak near the road centerline. In the future, the process  
of physical and chemical changes of particulate matter near the vehicle exhaust outlet should be further investigated.

465

### Data availability

Data are available upon request from the corresponding author Huan Liu ([liu\\_env@tsinghua.edu.cn](mailto:liu_env@tsinghua.edu.cn)).

### Code availability

470 Codes used during the current study are available from the corresponding author on reasonable request.

### Acknowledgment

We would like to acknowledge professor Jian Hang from Sun Yat-sen University for supports for CFD  
simulations and Dr. Jaime Benavides from Barcelona Supercomputing Center for the application of urban  
475 thermodynamic schemes. This work is supported by the National Natural Science Foundation of China (grant nos.  
41822505 and 42061130213 to H.L.), the Tsinghua–Toyota General Research Center. H.L. is supported by the  
Royal Society of the United Kingdom through a Newton Advanced Fellowship (NAF\R1\201166).

### Author contributions

480 Z. Lv and Z. Luo contributed equally. Z. Lv and Z. Luo designed the research and wrote the manuscript. H.L.  
provided guidance on the research and revised the paper. Z. Lv, Z. Luo, and F.D. provided multiple analytical



perspective on this research. X.W., J.Z., and L.X. helped collect and clean the data. T.H. helped on language modification.

#### 485 **Additional information**

Supplementary information is available for this paper at online resources.

Correspondence and requests for materials should be addressed to H.L.

#### **References**

- 490 An, Z., Huang, R.-J., Zhang, R., Tie, X., Li, G., Cao, J., Zhou, W., Shi, Z., Han, Y., Gu, Z., and Ji, Y.: Severe haze in northern China: A synergy of anthropogenic emissions and atmospheric processes, *Proceedings of the National Academy of Sciences of the United States of America*, 116, 8657-8666, 10.1073/pnas.1900125116, 2019.
- Benavides, J., Snyder, M., Guevara, M., Soret, A., Pérez García-Pando, C., Amato, F., Querol, X., and Jorba, O.: CALIOPE-Urban v1.0: coupling R-LINE with a mesoscale air quality modelling system for urban air quality forecasts over Barcelona city (Spain), *Geosci. Model Dev.*, 12, 2811-2835, 10.5194/gmd-12-2811-2019, 2019.
- 495 Breiman, L.: Random Forests, *Machine Learning*, 45, 5-32, 10.1023/A:1010933404324, 2001.
- Brown, M., Lawson, R., DeCroix, D., and Lee, R.: COMPARISON OF CENTERLINE VELOCITY MEASUREMENTS OBTAINED AROUND 2D AND 3D BUILDING ARRAYS IN A WIND TUNNEL, 2001.
- Byun, D. and Schere, K. L.: Review of the Governing Equations, Computational Algorithms, and Other Components of the Models-3 Community Multiscale Air Quality (CMAQ) Modeling System, *Applied Mechanics Reviews*, 59, 51-77, 10.1115/1.2128636, 2006.
- 500 Cheng, J., Su, J., Cui, T., Li, X., Dong, X., Sun, F., Yang, Y., Tong, D., Zheng, Y., Li, Y., Li, J., Zhang, Q., and He, K.: Dominant role of emission reduction in PM<sub>2.5</sub> air quality improvement in Beijing during 2013–2017: a model-based decomposition analysis, *Atmos. Chem. Phys.*, 19, 6125-6146, 10.5194/acp-19-6125-2019, 2019.
- 505 Cimarelli, A. J., Perry, S. G., Venkatram, A., Weil, J. C., Paine, R. J., Wilson, R. B., Lee, R. F., Peters, W. D., and Brode, R. W.: AERMOD: A Dispersion Model for Industrial Source Applications. Part I: General Model Formulation and Boundary Layer Characterization, *Journal of Applied Meteorology*, 44, 682-693, 10.1175/JAM2227.1, 2005.
- Cui, Y., Wang, L., Jiang, L., Liu, M., Wang, J., Shi, K., and Duan, X.: Dynamic spatial analysis of NO<sub>2</sub> pollution over China: Satellite observations and spatial convergence models, *Atmospheric Pollution Research*, 12, 89-99, 510 <https://doi.org/10.1016/j.apr.2021.02.003>, 2021.
- FLUENT: FLUENT V6.3. User's Manual. Available online: <http://www.fluent.com> (accessed on 20 August 2017). 2006.
- Foken, T.: 50 Years of the Monin–Obukhov Similarity Theory, *Boundary-Layer Meteorology*, 119, 431-447, 10.1007/s10546-006-9048-6, 2006.
- 515 Franke, J., Hellsten, A., Schlunzen, K. H., and Carissimo, B.: The COST 732 Best Practice Guideline for CFD simulation of flows in the urban environment: a summary, *International Journal of Environment and Pollution*, 44, 419-427, 10.1504/IJEP.2011.038443, 2011.
- Fu, X., Liu, J., Ban-Weiss, G. A., Zhang, J., Huang, X., Ouyang, B., Popoola, O., and Tao, S.: Effects of canyon geometry on the distribution of traffic-related air pollution in a large urban area: Implications of a multi-canyon air pollution dispersion model, *Atmospheric Environment*, 165, 111-121, <https://doi.org/10.1016/j.atmosenv.2017.06.031>, 2017.
- 520 Grell, G. A., Peckham, S. E., Schmitz, R., McKeen, S. A., Frost, G., Skamarock, W. C., and Eder, B.: Fully coupled “online” chemistry within the WRF model, *Atmospheric Environment*, 39, 6957-6975, <https://doi.org/10.1016/j.atmosenv.2005.04.027>, 2005.
- Hagler, G. S. W., Thoma, E. D., and Baldauf, R. W.: High-Resolution Mobile Monitoring of Carbon Monoxide and Ultrafine Particle Concentrations in a Near-Road Environment, *Journal of the Air & Waste Management Association*, 60, 328-336, 525 10.3155/1047-3289.60.3.328, 2012.
- Hang, J., Sandberg, M., Li, Y., and Claesson, L.: Flow mechanisms and flow capacity in idealized long-street city models,



- Building and Environment, 45, 1042-1053, <https://doi.org/10.1016/j.buildenv.2009.10.014>, 2010.
- 530 He, J., Wu, L., Mao, H., Liu, H., Jing, B., Yu, Y., Ren, P., Feng, C., and Liu, X.: Development of a vehicle emission inventory with high temporal–spatial resolution based on NRT traffic data and its impact on air pollution in Beijing – Part 2: Impact of vehicle emission on urban air quality, *Atmos. Chem. Phys.*, 16, 3171-3184, 10.5194/acp-16-3171-2016, 2016.
- Jin, Y., Andersson, H., and Zhang, S.: Air Pollution Control Policies in China: A Retrospective and Prospects, *International Journal of Environmental Research and Public Health*, 13, 1219, 2016.
- 535 Kakosimos, K. E., Hertel, O., Ketzler, M., and Berkowicz, R.: Operational Street Pollution Model (OSPM) – a review of performed application and validation studies, and future prospects, *Environmental Chemistry*, 7, 485-503, <https://doi.org/10.1071/EN10070>, 2010.
- Ke, W., Zhang, S., Wu, Y., Zhao, B., Wang, S., and Hao, J.: Assessing the Future Vehicle Fleet Electrification: The Impacts on Regional and Urban Air Quality, *Environmental Science & Technology*, 51, 1007-1016, 10.1021/acs.est.6b04253, 2017.
- 540 Khaniabadi, Y. O., Goudarzi, G., Daryanoosh, S. M., Borgini, A., Tittarelli, A., and De Marco, A.: Exposure to PM10, NO2, and O3 and impacts on human health, *Environmental Science and Pollution Research*, 24, 2781-2789, 10.1007/s11356-016-8038-6, 2017.
- Kheirbek, I., Haney, J., Douglas, S., Ito, K., and Matte, T.: The contribution of motor vehicle emissions to ambient fine particulate matter public health impacts in New York City: a health burden assessment, *Environmental Health*, 15, 89, 10.1186/s12940-016-0172-6, 2016.
- 545 Kikumoto, H., Ooka, R., Sugawara, H., and Lim, J.: Observational study of power-law approximation of wind profiles within an urban boundary layer for various wind conditions, *Journal of Wind Engineering and Industrial Aerodynamics*, 164, 13-21, <https://doi.org/10.1016/j.jweia.2017.02.003>, 2017.
- Kim, Y., Wu, Y., Seigneur, C., and Roustan, Y.: Multi-scale modeling of urban air pollution: development and application of a Street-in-Grid model (v1.0) by coupling MUNICH (v1.0) and Polair3D (v1.8.1), *Geosci. Model Dev.*, 11, 611-629, 10.5194/gmd-11-611-2018, 2018.
- 550 Liaw, A., Wiener, M.: Classification and regression by randomForest, *R News*, 2, 18–22, 2002.
- Lien, F.-S. and Yee, E.: Numerical Modelling of the Turbulent Flow Developing Within and Over a 3-D Building Array, Part I: A High-Resolution Reynolds-Averaged Navier–Stokes Approach, *Boundary-Layer Meteorology*, 112, 427-466, 10.1023/B:BOUN.0000030654.15263.35, 2004.
- 555 Luo, Z., Xu, H., Zhang, Z., Zheng, S., and Liu, H.: Year-round changes in tropospheric nitrogen dioxide caused by COVID-19 in China using satellite observation, *Journal of Environmental Sciences*, <https://doi.org/10.1016/j.jes.2022.01.013>, 2022a.
- Luo, Z., Wang, Y., Lv, Z., He, T., Zhao, J., Wang, Y., Gao, F., Zhang, Z., and Liu, H.: Impacts of vehicle emission on air quality and human health in China, *Science of The Total Environment*, 813, 152655, <https://doi.org/10.1016/j.scitotenv.2021.152655>, 2022b.
- 560 Lv, Z., Wang, X., Deng, F., Ying, Q., Archibald, A. T., Jones, R. L., Ding, Y., Cheng, Y., Fu, M., Liu, Y., Man, H., Xue, Z., He, K., Hao, J., and Liu, H.: Source–Receptor Relationship Revealed by the Halted Traffic and Aggravated Haze in Beijing during the COVID-19 Lockdown, *Environmental Science & Technology*, 54, 15660-15670, 10.1021/acs.est.0c04941, 2020.
- Greenwell B M.: pdp: An R Package for Constructing Partial Dependence Plots, *R Journal*, 9(1): 421., 2017.
- Manning, A. J., Nicholson, K. J., Middleton, D. R., and Rafferty, S. C.: Field Study of Wind and Traffic to Test a Street Canyon Pollution Model, *Environmental Monitoring and Assessment*, 60, 283-313, 10.1023/A:1006187301966, 2000.
- 565 Masey, N., Hamilton, S., and Beverland, I. J.: Development and evaluation of the RapidAir® dispersion model, including the use of geospatial surrogates to represent street canyon effects, *Environmental Modelling & Software*, 108, 253-263, <https://doi.org/10.1016/j.envsoft.2018.05.014>, 2018.
- MEPC: Ambient Air Quality Standard, 2012.
- 570 Murena, F., Favale, G., Vardoulakis, S., and Solazzo, E.: Modelling dispersion of traffic pollution in a deep street canyon: Application of CFD and operational models, *Atmospheric Environment*, 43, 2303-2311, <https://doi.org/10.1016/j.atmosenv.2009.01.038>, 2009.
- Nayeb Yazdi, M., Delavarrafiee, M., and Arhami, M.: Evaluating near highway air pollutant levels and estimating emission factors: Case study of Tehran, Iran, *Science of The Total Environment*, 538, 375-384, <https://doi.org/10.1016/j.scitotenv.2015.07.141>, 2015.
- 575 Nguyen, C., Soulhac, L., and Salizzoni, P.: Source Apportionment and Data Assimilation in Urban Air Quality Modelling for NO2: The Lyon Case Study, *Atmosphere*, 9, 10.3390/atmos9010008, 2018.



- Oke, T. R.: Street design and urban canopy layer climate, *Energy and Buildings*, 11, 103-113, [https://doi.org/10.1016/0378-7788\(88\)90026-6](https://doi.org/10.1016/0378-7788(88)90026-6), 1988.
- 580 Pandey, J. S., Kumar, R., and Devotta, S.: Health risks of NO<sub>2</sub>, SPM and SO<sub>2</sub> in Delhi (India), *Atmospheric Environment*, 39, 6868-6874, <https://doi.org/10.1016/j.atmosenv.2005.08.004>, 2005.
- Patterson, R. F. and Harley, R. A.: Evaluating near-roadway concentrations of diesel-related air pollution using RLINE, *Atmospheric Environment*, 199, 244-251, <https://doi.org/10.1016/j.atmosenv.2018.11.016>, 2019.
- Shah, V., Jacob, D. J., Li, K., Silvern, R. F., Zhai, S., Liu, M., Lin, J., and Zhang, Q.: Effect of changing NO<sub>x</sub> lifetime on the seasonality and long-term trends of satellite-observed tropospheric NO<sub>2</sub> columns over China, *Atmos. Chem. Phys.*, 20, 1483-1495, 10.5194/acp-20-1483-2020, 2020.
- 585 Snyder, M. G., Venkatram, A., Heist, D. K., Perry, S. G., Petersen, W. B., and Isakov, V.: RLINE: A line source dispersion model for near-surface releases, *Atmospheric Environment*, 77, 748-756, <https://doi.org/10.1016/j.atmosenv.2013.05.074>, 2013.
- Soulhac, L., Perkins, R. J., and Salizzoni, P.: Flow in a Street Canyon for any External Wind Direction, *Boundary-Layer Meteorology*, 126, 365-388, 10.1007/s10546-007-9238-x, 2008.
- 590 Soulhac, L., Nguyen, C., Volta, P., and Salizzoni, P.: The model SIRANE for atmospheric urban pollutant dispersion. PART III: Validation against NO<sub>2</sub> yearly concentration measurements in a large urban agglomeration, *Atmospheric Environment*, 167, 10.1016/j.atmosenv.2017.08.034, 2017.
- Soulhac, L., Salizzoni, P., Mejean, P., Didier, D., and Rios, I.: The model SIRANE for atmospheric urban pollutant dispersion; PART II, validation of the model on a real case study, *Atmospheric Environment*, 49, 320-337, <https://doi.org/10.1016/j.atmosenv.2011.11.031>, 2012.
- 595 Tominaga, Y., Mochida, A., Yoshie, R., Kataoka, H., Nozu, T., Yoshikawa, M., and Shirasawa, T.: AIJ guidelines for practical applications of CFD to pedestrian wind environment around buildings, *Journal of Wind Engineering and Industrial Aerodynamics*, 96, 1749-1761, <https://doi.org/10.1016/j.jweia.2008.02.058>, 2008.
- 600 Vara-Vela, A., Andrade, M. F., Kumar, P., Ynoue, R. Y., and Muñoz, A. G.: Impact of vehicular emissions on the formation of fine particles in the Sao Paulo Metropolitan Area: a numerical study with the WRF-Chem model, *Atmos. Chem. Phys.*, 16, 777-797, 10.5194/acp-16-777-2016, 2016.
- Yu, M., Zhu, Y., Lin, C.-J., Wang, S., Xing, J., Jang, C., Huang, J., Huang, J., Jin, J., and Yu, L.: Effects of air pollution control measures on air quality improvement in Guangzhou, China, *Journal of Environmental Management*, 244, 127-137, <https://doi.org/10.1016/j.jenvman.2019.05.046>, 2019.
- 605 Zhang, K., Chen, G., Wang, X., Liu, S., Mak, C. M., Fan, Y., and Hang, J.: Numerical evaluations of urban design technique to reduce vehicular personal intake fraction in deep street canyons, *Science of The Total Environment*, 653, 968-994, <https://doi.org/10.1016/j.scitotenv.2018.10.333>, 2019a.
- Zhang, Q., Tong, P., Liu, M., Lin, H., Yun, X., Zhang, H., Tao, W., Liu, J., Wang, S., Tao, S., and Wang, X.: A WRF-Chem model-based future vehicle emission control policy simulation and assessment for the Beijing-Tianjin-Hebei region, China, *Journal of Environmental Management*, 253, 109751, <https://doi.org/10.1016/j.jenvman.2019.109751>, 2020.
- 610 Zhang, Q., Zheng, Y., Tong, D., Shao, M., Wang, S., Zhang, Y., Xu, X., Wang, J., He, H., Liu, W., Ding, Y., Lei, Y., Li, J., Wang, Z., Zhang, X., Wang, Y., Cheng, J., Liu, Y., Shi, Q., Yan, L., Geng, G., Hong, C., Li, M., Liu, F., Zheng, B., Cao, J., Ding, A., Gao, J., Fu, Q., Huo, J., Liu, B., Liu, Z., Yang, F., He, K., and Hao, J.: Drivers of improved PM<sub>2.5</sub> air quality in China from 2013 to 2017, *Proceedings of the National Academy of Sciences*, 116, 24463-24469, 10.1073/pnas.1907956116, 2019b.
- 615 Zhang, Y., Ye, X., Wang, S., He, X., Dong, L., Zhang, N., Wang, H., Wang, Z., Ma, Y., Wang, L., Chi, X., Ding, A., Yao, M., Li, Y., Li, Q., Zhang, L., and Xiao, Y.: Large-eddy simulation of traffic-related air pollution at a very high resolution in a megacity: evaluation against mobile sensors and insights for influencing factors, *Atmos. Chem. Phys.*, 21, 2917-2929, 10.5194/acp-21-2917-2021, 2021.
- 620 Zheng, B., Tong, D., Li, M., Liu, F., Hong, C., Geng, G., Li, H., Li, X., Peng, L., Qi, J., Yan, L., Zhang, Y., Zhao, H., Zheng, Y., He, K., and Zhang, Q.: Trends in China's anthropogenic emissions since 2010 as the consequence of clean air actions, *Atmos. Chem. Phys.*, 18, 14095-14111, 10.5194/acp-18-14095-2018, 2018.
- Zhu, Y., Zhan, Y., Wang, B., Li, Z., Qin, Y., and Zhang, K.: Spatiotemporally mapping of the relationship between NO<sub>2</sub> pollution and urbanization for a megacity in Southwest China during 2005–2016, *Chemosphere*, 220, 155-162, <https://doi.org/10.1016/j.chemosphere.2018.12.095>, 2019.
- 625

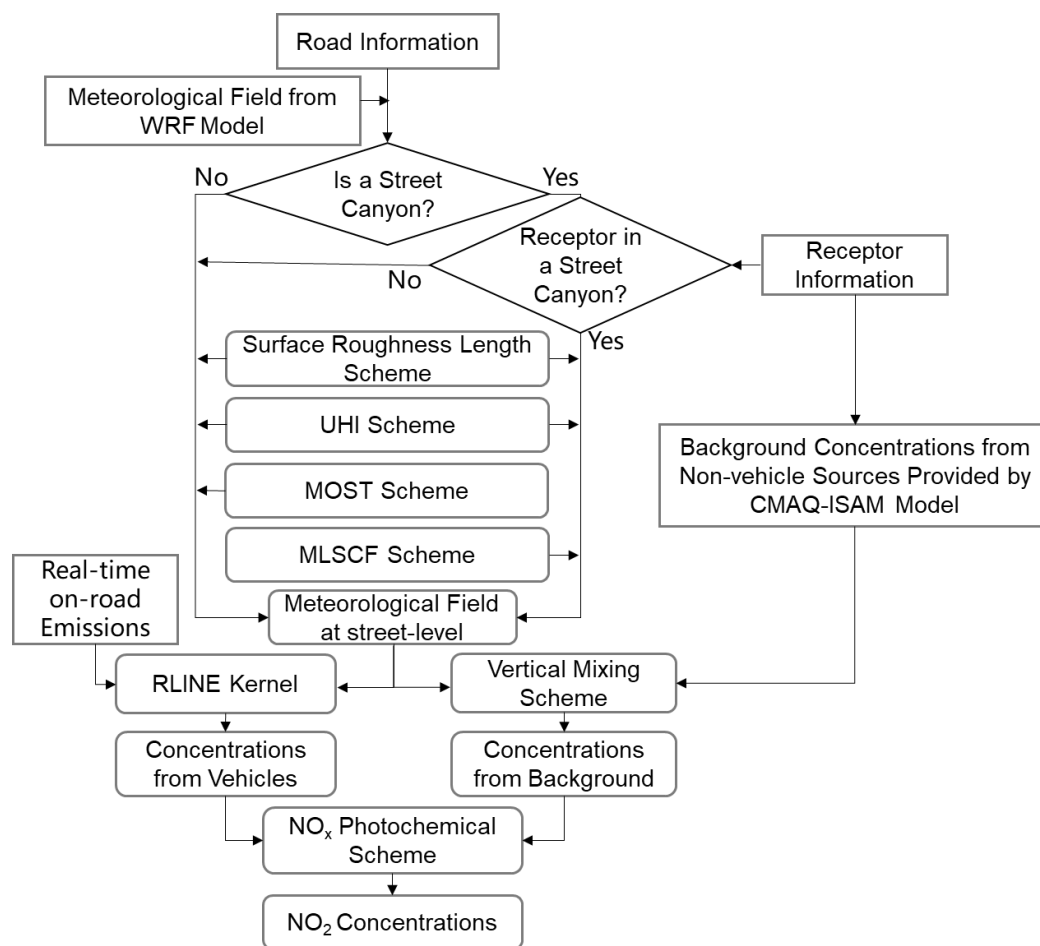


**Figure 1: The framework of multiscale hybrid model CMAQ-RLINE\_URBAN.**

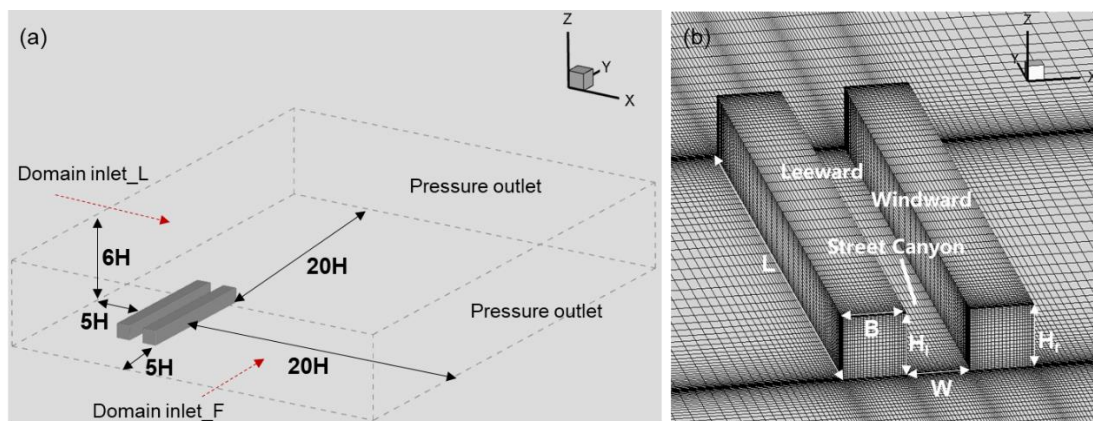


**Figure 2: Computational domain and grid arrangement in all CFD test case. (a) Settings of CFD simulation domain and (b) control factors.**

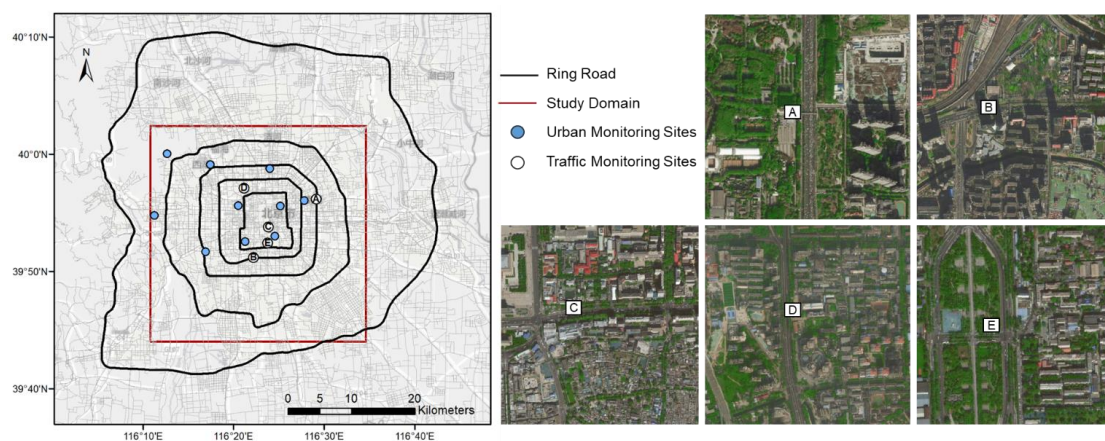


**Figure 3: Study domain (© OpenStreetMap contributors 2020. Distributed under the Open Data Commons Open Database License (ODbL) v1.0) and location of monitoring sites (© Microsoft). A. DSH; B. NSH; C. QM; D. XZM; E. YDM.**

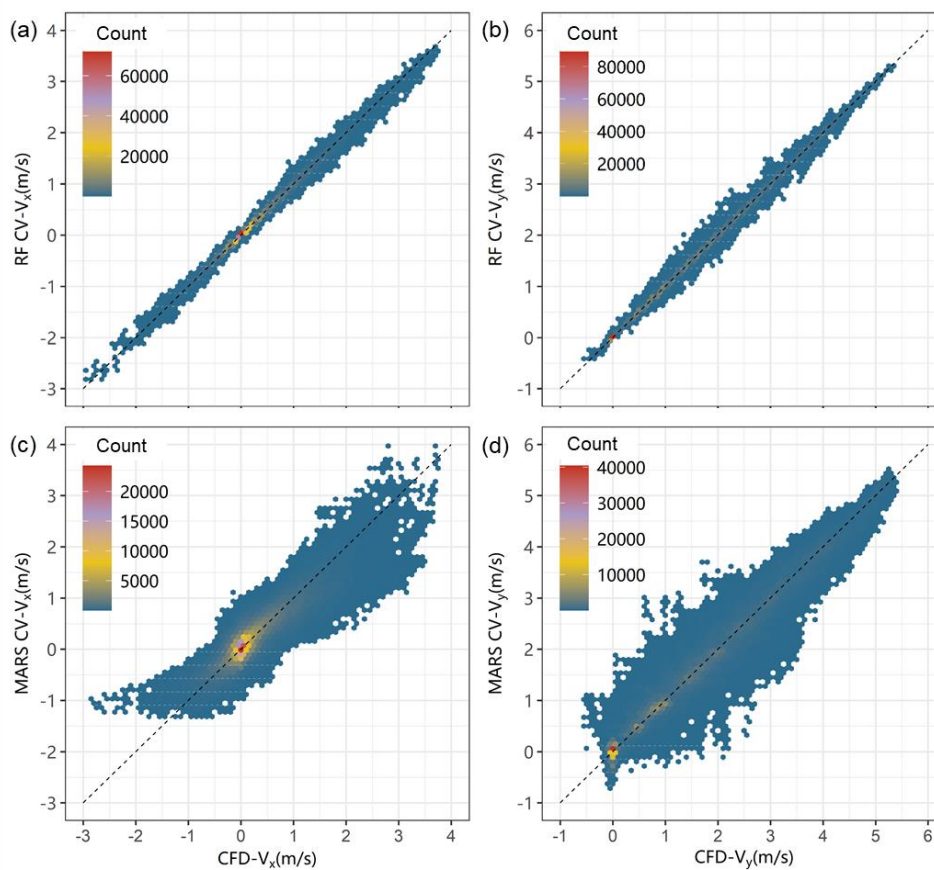
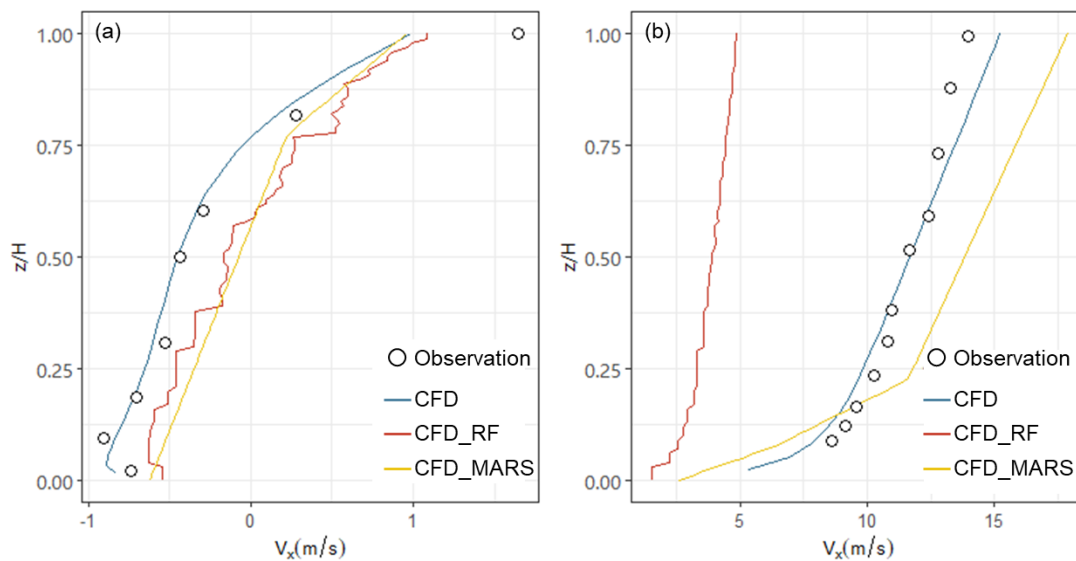


**Figure 4: Cross validations of machine learning models for  $V_x$  (a, c) and  $V_y$  (b, d): (a)-(b) RF model; (c)-(d) MARS model.**





645

**Figure 5: Performances of machine learning on velocity profile in different wind tunnel experiments.**

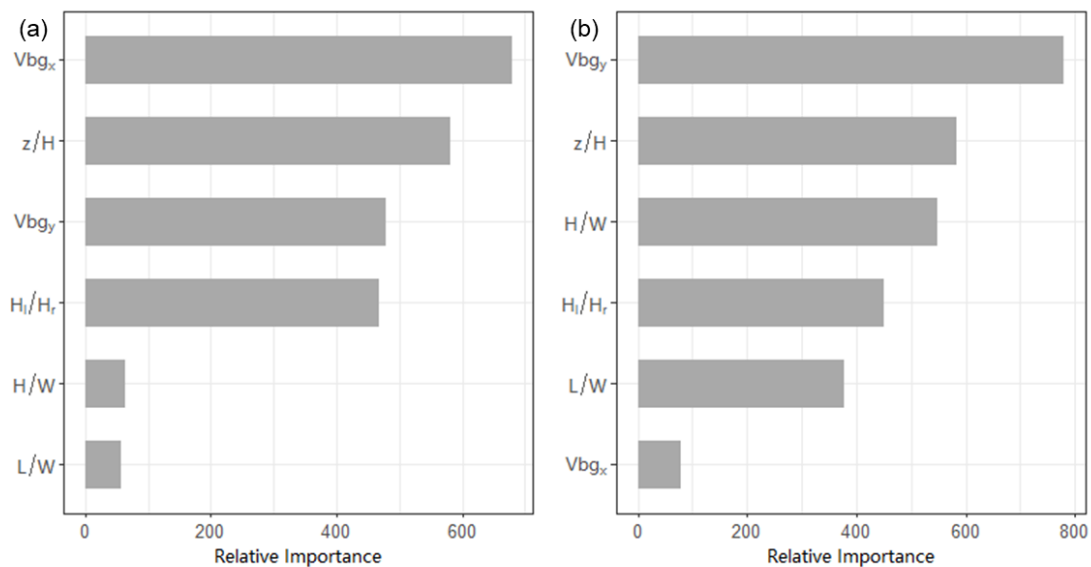
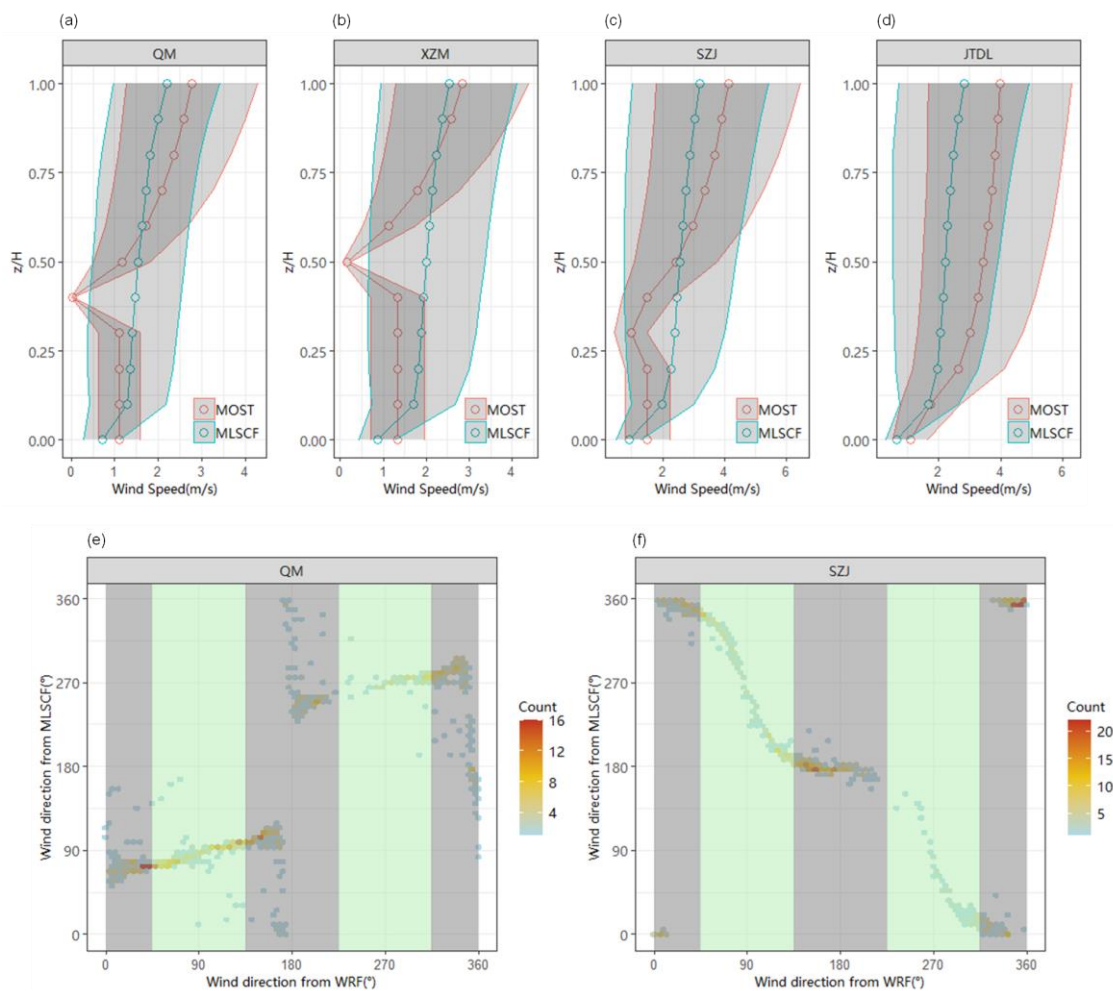
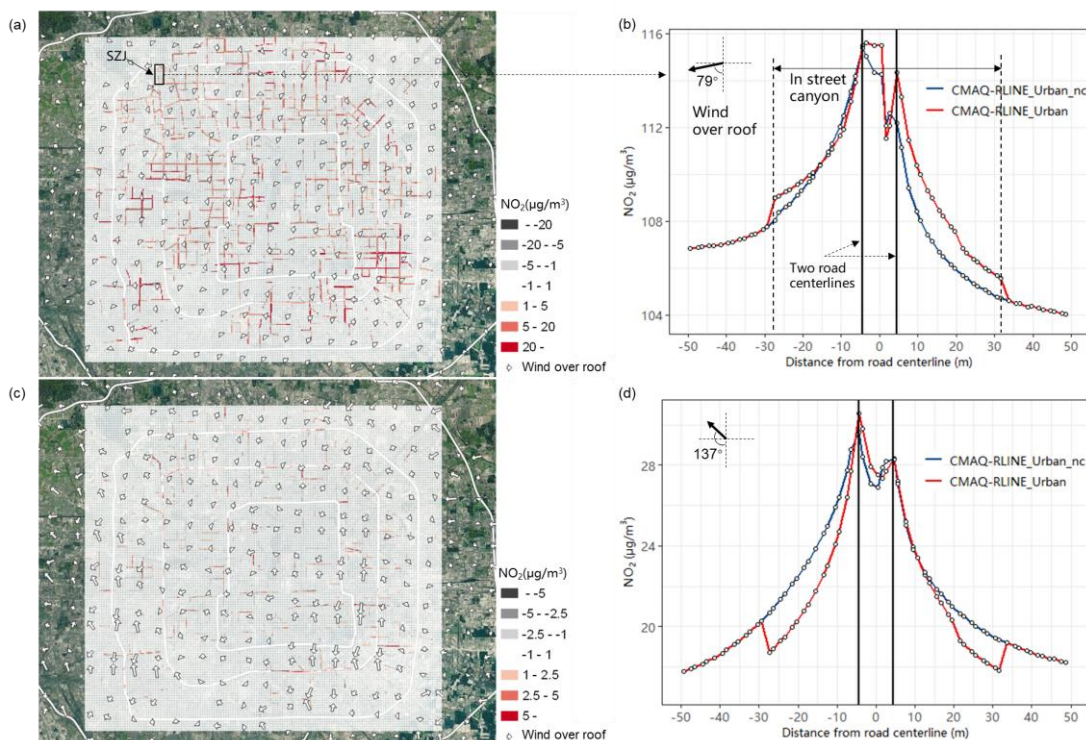


**Figure 6: Variable importance ranking in the RF model for (a)  $V_x$  and (b)  $V_y$ .**

650

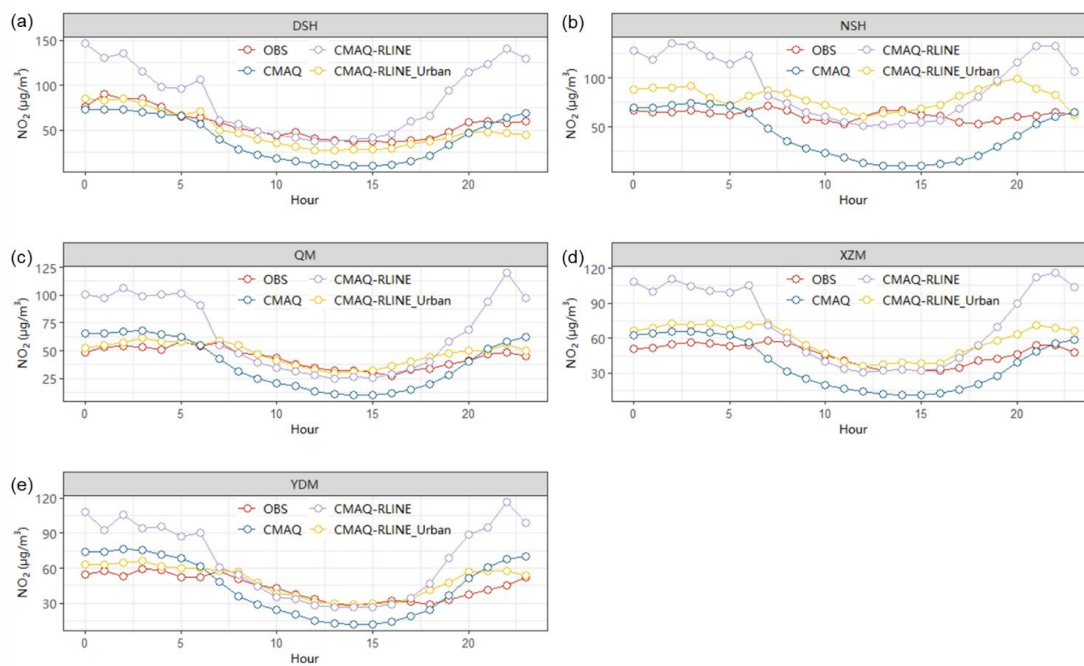


655 **Figure 7: Influence of MLSCF on wind field in the street canyon. Monthly averaged vertical profile of wind speed from MOST and MLSCF method in different street canyons: (a) QM (H/W=0.22); (b) XZM (H/W=0.35); (c) SZJ (H/W=1); (b) JTDL (H/W=1.93). The gray shade represents the standard deviation in results of all hours. Hourly wind direction from WRF model (at roof level) and MLSCF method (at ground level) in different street canyons. (e) QM (H/W=0.22); (f) SZJ (H/W=1). As the gray and green shade shown, the background wind over the street canyon provided by WRF model was divided into four main directions: east, west, south and north.**



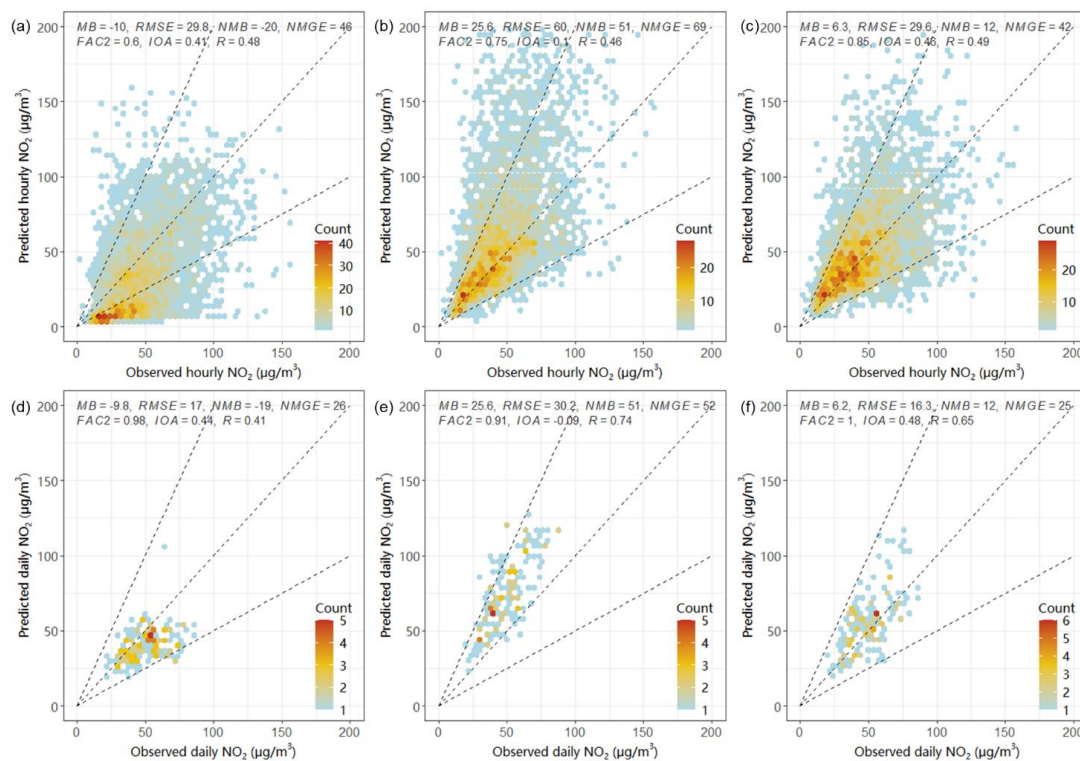
660

**Figure 8: Differences in NO<sub>2</sub> concentrations at the height of 1.5 m impacted by MLSCF scheme (a, c) over the study domain (CMAQ-RLINE\_URBAN - CMAQ-RLINE\_URBAN\_nc) (© Microsoft) and (b, d) near SZJ in 2019-08-24 at 0:00-1:00 (a, b) and 10:00-11:00 (c, d).**



665

**Figure 9: Diurnal variations of observed and predicted hourly averaged NO<sub>2</sub> concentrations from different models at near-road monitoring sites: (a) DSH; (b) NSH; (c) QM; (d) XZM; (e) YDM.**



670 **Figure 10: Observed and predicted hourly (a-c) or daily averaged (d-f) NO<sub>2</sub> concentrations from different models at near-road sites: (a, d) CMAQ model; (b, e) CMAQ-RLINE model; (c, f) CMAQ-RLINE\_URBAN model.**



675

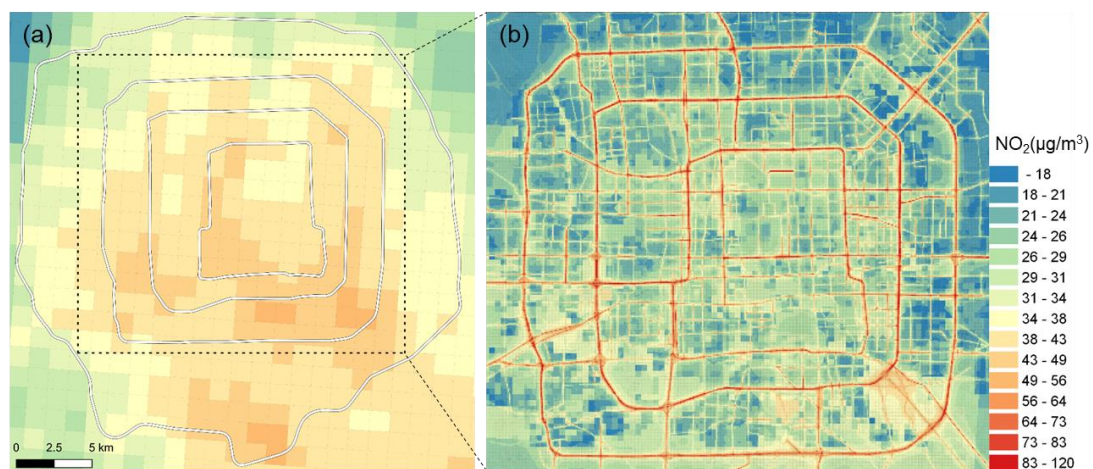
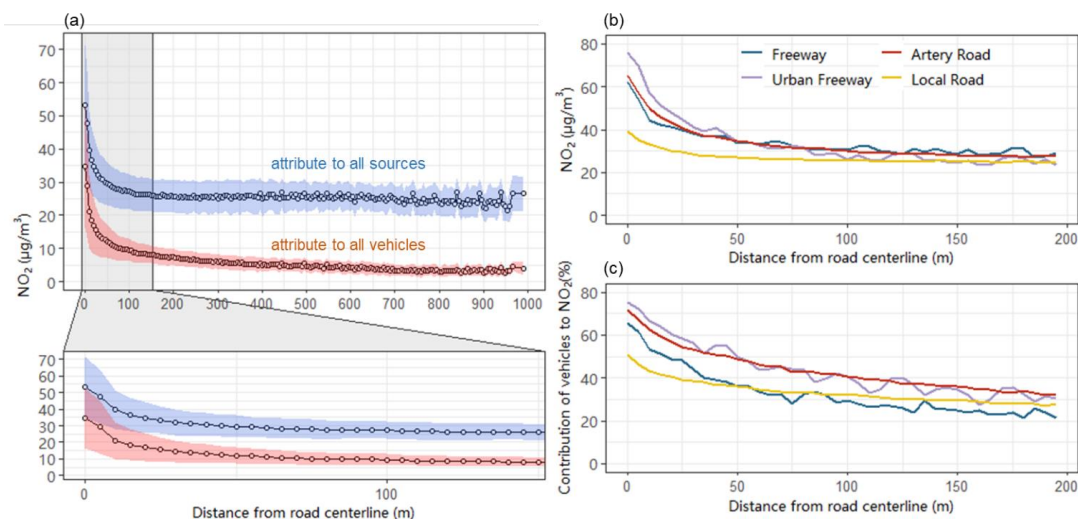


**Figure 11: Spatial distribution of monthly averaged NO<sub>2</sub> concentrations from (a) CMAQ model and (b) CMAQ-RLINE\_URBAN model.**



680

**Figure 12: Monthly averaged NO<sub>2</sub> concentrations attributed to all sources or vehicles with distance from the receptor to its nearest road centerline. (a) NO<sub>2</sub> attributed to all sources near all roads; (b) NO<sub>2</sub> attributed to all sources near different road types; (c) Relative contribution of vehicles to NO<sub>2</sub> near different road types. The shade area in (a) represents the standard deviation in results of all receptors.**

685





**Table 1: Values of controlling factors used in the simulations.**

Controlling factor	Value				
$H_l/H_r$ (unitless)	0.50	0.75	1.00	1.33	2.00
$H/W$ (unitless)	0.25	0.50	1.00	2.00	-
$L/H$ (unitless)	3	5	10	20	-
$V(H)$ (m/s)	1	2	3	4	5
$\alpha$ (°)	0	30	60	90	-



**Table 2: Model performances under different scenarios**

Sites	Scenario	MB	RMSE	NMB	NMGE	FAC2	IOA	R
All	CMAQ	3.1	25.6	9	53	0.65	0.45	0.52
	CMAQ-RLINE	18.5	46.6	53	77	0.67	0.19	0.55
	CMAQ-RLINE_URBAN	4.6	25.8	13	49	0.75	0.49	0.57
Urban	CMAQ	8.0	24.3	27	58	0.68	0.40	0.59
	CMAQ-RLINE	12.3	35.8	43	76	0.64	0.20	0.50
	CMAQ-RLINE_URBAN	1.3	23.1	4	51	0.71	0.47	0.49

690 \*MB: Mean bias; RSME: Root mean squared error; NMB: Normalized mean bias; NMGE: Normalized mean gross error; FAC2: Fraction of predictions within a factor of two; IOA: Index of agreement; R: correlation coefficient.